A finite-element reciprocity solution for EEG forward modeling with realistic individual head models

Erik Ziegler[a,*], Sarah L. Chellappa[a], Giulia Gaggioni[a], Julien Q. M. Ly[a], Gilles Vandewalle[a], Elodie André[a], Christophe Geuzaine[b,1], Christophe Phillips[a,b,1]

[a] *Cyclotron Research Centre, University of Liège, Liège, Belgium*
[b] *Department of Electrical Engineering and Computer Science, University of Liège, Liège, Belgium*

Abstract

We present a finite element modeling (FEM) implementation for solving the forward problem in electroencephalography (EEG). The solution is based on Helmholtz's principle of reciprocity which allows for dramatically reduced computational time when constructing the leadfield matrix. The approach was validated using a 4-shell spherical model and shown to perform comparably with two current state-of-the-art alternatives (OpenMEEG for boundary element modeling and SimBio for finite element modeling).

We applied the method to real human brain MRI data and created a model with five tissue types: white matter, grey matter, cerebrospinal fluid, skull, and scalp. By calculating conductivity tensors from diffusion-weighted MR images, we also demonstrate one of the main benefits of FEM: the ability to include anisotropic conductivities within the head model. Root-mean square deviation between the standard leadfield and the leadfield including white-matter anisotropy showed that ignoring the directional conductivity of white matter fiber tracts leads to orientation-specific errors in the forward model.

Realistic head models are necessary for precise source localization in individuals. Our approach is fast, accurate, open-source and freely available online.

Keywords: electroencephalography, EEG, forward model, diffusion

*Corresponding author
Email address: erik.ziegler@ulg.ac.be (Erik Ziegler)
[1] Contributed equally

Introduction

Identifying the sources of neuronal activity is a key step in many studies using electroencephalography (EEG) or magnetoencephalography (MEG). The problem itself is ill-posed as there can be an infinite number of solutions describing the origin of the neural activity that has been recorded [1]. There are two problems to solve if one wants to identify the location of neuronal activity from a set of electrode recordings. The first is known as the forward problem, and its basis is building an electromagnetic model of the subject's head. Once this is created, one can attempt to identify neural sources by solving the inverse problem. The inverse problem is essentially an optimization problem, where the procedure is to work backwards from the scalp recordings in order to identify one or more current dipoles which best explain the acquired data. In this paper we focus on the forward problem, which has not been given a great deal of attention in neuroimaging. Despite many published studies demonstrating high-quality head models and forward modeling approaches [2, 3, 4, 5, 6, 7, 8], most functional neuroimaging studies still rely on relatively poor quality electromagnetic head models when performing source localization.

There are generally three types of head modeling methods. The first and easiest is the simplification of the head to a spherical model. The second, and most common, is boundary element modeling (BEM), in which distinct shells of the head are meshed as two-dimensional surfaces and the volume in between them is treated as distinct tissue types (e.g. BEM meshes may represent the inner and outer borders of the skull). The third is finite element modeling (FEM), which operates similarly to boundary element modeling with the exception that meshes are constructed in three dimensions (e.g. using tetrahedra).

Researchers have learned to avoid oversimplified spherical head models, and most now use boundary element solutions built-in to packages like SPM [9], NFT [10], MNE [11, 12], and OpenMEEG [13]. Boundary element models are known to perform quickly and with high accuracy, though they suffer some drawbacks due to their geometric limitations. Simply put, these methods fail in situations with complex geometries. Their largest fault is that they assume isotropic conductivity within all regions of each tissue type, an assumption that is well known to be incorrect [13]. Although efforts have been made to include

anisotropic conductivity into BEM methods [14], it is technically very challenging.

Approaches for solving the forward problem aim to create what is known as a leadfield matrix. The leadfield matrix allows for the computation of the potential distribution on the sensors from a current source (e.g. synchronously firing neurons) placed inside the brain. The relationship between the leadfield matrix (L) and the remainder of the system can be written as:

$$\Phi = L \cdot j + n \tag{1}$$

Where Φ is the recorded sensor potential, j is the neural source represented as a current dipole, and n represents the noise in the system. An analytical solution has been derived for obtaining the potential distribution on the surface of an ellipsoid given an arbitrarily located current dipole [15, 16, 17]. The analytical approach is used as the ground truth when testing new methods.

The most common approach to computing the leadfield, known as the direct method, is to place several thousand current dipoles in the brain within the cortical ribbon, oriented tangentially to the white matter surface. For each dipole, the scalp potential is obtained by solving the forward problem. The leadfield matrix is then created from the chosen dipole positions and the calculated sensor potentials. Realistic finite element (FE) models of the human head require hundreds of thousands of elements to provide accurate solutions. Due to the high mesh complexity, the typical direct method for computing the leadfield matrix becomes unreasonably slow for finite element models. To overcome this, alternative methods for calculating the leadfield matrix, such as the adjoint[18], subtraction [19, 20], and reciprocity [21, 22] approaches have been devised. The approach taken here was derived from Helmholtz's principle of reciprocity and first applied to EEG by Rush and Driscoll [1, 21]. Reciprocity explains that the roles of the dipole and sensor can be reversed, compared to the direct method. A full leadfield matrix can be created by applying current between each sensor and a ground electrode, and storing the electric field induced in each element of the head model. In this framework only $M-1$ iterations of the forward problem are necessary to create a leadfield matrix, where M is the number of sensors. The direct method, in contrast, requires thousands of iterations to create a leadfield

from a dense array of sources. A number of previous studies have demonstrated the use of reciprocity for FEM solutions [22, 2, 3, 7]. This article draws heavily on the work of Weinstein et al. for its basis [22].

It is well known that white matter fiber structures in the human brain are highly directional (i.e. anisotropic) in both their structure and properties. Diffusion-weighted imaging (DWI) allows for the quantification and modeling of water movement within tissues and can be used to compute the anisotropy profile of brain structures (e.g. by fitting a tensor at each voxel) [23]. It has also been established that through a remapping of the tensor's eigenvalues, electrical conductivity can be approximated from the water diffusion tensor [24]. This allows finite element models to include local information about the conductivity of the tissues which boundary element methods are incapable of integrating.

To our knowledge there is currently only one freely available solution for realistic FEM forward modeling - NeuroFEM, part of SimBio [25]. The developers of NeuroFEM have created a number of forward solvers and efforts are underway to bring an easily accessible wrapper to MATLAB through integration with Fieldtrip [26]. The installation and use NeuroFEM remains complex, though, as it must be compiled directly by the user, and this is often non-trivial on modern operating systems. SimBio also relies on many outdated file formats which makes interoperability difficult. There is also no standard or reproducible meshing procedure available in SimBio; in recent publications skin and skull meshing has been performed, at least in part, using commercial software [8, 27].

We therefore aimed to create an alternative toolbox for accurate and fast subject-specific finite element modeling in EEG studies. The approach was evaluated using a four-shell spherical model and real data from a human subject. We have developed our software in the open under a free software license and welcome contributions from the community (see Technical Details).

Methods

We have split the methods section into three parts. The first describes our implementation and approach to calculating the leadfield matrix. The second section describes our evaluation of the approach against the analytical solution

using a four-shell spherical model. The third section details our tests with real-world MRI and DWI data.

Finite element reciprocity solution

In neuroscience patches of active cortex are often approximated as dipolar current sources with extremely small distances between their poles. These equivalent current dipoles have three-dimensional orientations and units of current times length ($A \cdot m$). The reciprocity principle explains that in order to identify the voltage (ϕ) difference between any two points resulting from a single current dipole (j), it is sufficient to know the electric field (E) at the dipole location produced by injecting a known current (I) through two points (A, B).

$$\phi_A - \phi_B = \frac{E \cdot j}{I} \tag{2}$$

This allows us to switch the role of the dipoles and sensors compared to the typical direct method. We place surface leads on the scalp and calculate the electric field in each element of the grey matter. Given a dipole location and orientation, using Equation 2 will provide us with each sensor potential, relative to a ground electrode.

The forward problem is redefined for each source electrode and the FEM calculations are performed using GetDP with the Galerkin approach. In-depth mathematical details can be found in the Supplementary Material. The current density, electric field, and potential are calculated at each element. The process of creating and comparing the leadfield matrix, in practice, is as follows:

1. An arbitrary ground electrode is chosen by the user.
2. A unit current source is defined at one of the (non-ground) sensor locations.
3. The induced electric field in each element of the 3D mesh is calculated with GetDP
4. Steps 2 and 3 are repeated for all non-ground sensors. The electric field vector for each element is stored and these rows are later stacked to create the leadfield matrix defined in Equation 3.
5. To calculate the potential on the sensors from a dipole at any given location, one must first identify the mesh element (N) closest to the dipole

location. The potential at each sensor caused by a dipole in that element is the dot product of the dipole orientation vector (j^N) and the leadfield vector (L^N) for the element (see Equation 1).

Once the leadfield is pre-computed, it is trivial to calculate the sensor potential produced by a dipole in any element.

$$\begin{bmatrix} L_1^{1,x} & L_1^{1,y} & L_1^{1,z} & \cdots & L_1^{N,x} & L_1^{N,y} & L_1^{N,z} \\ L_2^{1,x} & L_2^{1,y} & L_2^{1,z} & \cdots & L_2^{N,x} & L_2^{N,y} & L_2^{N,z} \\ \vdots & \vdots & \vdots & \vdots & \vdots & \vdots & \vdots \\ L_M^{1,x} & L_M^{1,y} & L_M^{1,z} & \cdots & L_M^{N,x} & L_M^{N,y} & L_M^{N,z} \end{bmatrix} \cdot \begin{bmatrix} j^{1,x} \\ j^{1,y} \\ j^{1,z} \\ \vdots \\ j^{N,x} \\ j^{N,y} \\ j^{N,z} \end{bmatrix} = \begin{bmatrix} \Phi_1 \\ \Phi_2 \\ \vdots \\ \Phi_M \end{bmatrix} \tag{3}$$

The benefits of reciprocity are clear, as the forward problem need only be solved $M-1$ times, where M is the number of EEG electrodes. In comparison, the standard direct method requires a dense array (usually thousands) of dipole sources (and independent calculations) throughout the grey matter.

Validation in a spherical model

In this section we compare our implementation with two other freely available solvers, OpenMEEG and SimBio. We calculate two parameters: the relative difference and relative magnitude. These parameters are used to describe the error between the numerically calculated solution and the analytically derived solution. The relative difference measure (RDM) is defined as:

$$RDM(\widetilde{\Phi}, \Phi_a) = ||\frac{\widetilde{\Phi}}{||\widetilde{\Phi}||} - \frac{\Phi_a}{||\Phi_a||}|| \tag{4}$$

Where $\widetilde{\Phi}$ represents the potential on the electrodes computed numerically, and Φ_a is the analytically calculated potential. The relative magnitude (MAG) between these values is calculated using Equation 5:

$$MAG(\widetilde{\Phi}, \Phi_a) = \frac{||\widetilde{\Phi}||}{||\Phi_a||} \tag{5}$$

In these equations the norm ($||\Phi||$) indicates the Euclidean (ℓ^2) norm over the recorded electrode measurements. Relative difference in magnitude (RDM) is better the closer it is to zero, whereas relative magnitude (MAG) should as close as possible to 1.

Four spherical 2D meshes were created in Gmsh and volumetric meshes were created between them. Volumes between the shells were considered to represent, from inside outward, (i) brain, (ii) cerebrospinal fluid, (iii) skull, and (iv) skin. The characteristic length of the triangular and tetrahedral elements was 3 mm in the brain and 7 mm in the cerebrospinal fluid, skull, and skin. In total the mesh contained 52,510 nodes and 336,000 elements. The same volumetric mesh was used for simulations performed in SimBio.

Electrode locations were selected by creating a unit icosahedron, scaling the vertex locations by the radius of the sphere (100 mm), and selecting the closest tetrahedra of the spherical mesh. The number of electrodes depends on the number of vertices in the icosahedron, which in this case was 42. The spherical model is shown in Figure 1 and the conductivity values used can be found in Table 1. A matching spherical boundary element model was created in OpenMEEG [13] and the leadfield was calculated. The boundary element model had 42 nodes and 80 triangles per spherical shell, for a total of 168 nodes and 320 elements. To enable comparison with the analytical solution, the leadfields from OpenMEEG and SimBio were re-referenced by subtracting the value at the user-selected ground electrode from all other electrode potentials. Probe dipoles were placed at distances 4 mm apart from the centre of the sphere up to the boundary between brain and CSF, oriented outwards, for a total of 22 probe positions. The RDM and MAG were calculated for OpenMEEG, SimBio, and our implementation.

Application to real data

Participants Written informed consent was obtained from our subject in accordance with the Declaration of Helsinki. The Ethics Committee of the University of Liège approved the study. Data used in the Supplementary Material was acquired at the University of Tübingen and is freely available online [28].

Images were acquired on a 3 T head-only MR scanner (Magnetom Allegra, Siemens Medical Solutions, Erlangen, Germany) operated with an 8-channel

head coil. Diffusion-weighted (DW) images were acquired with a twice-refocused spin-echo sequence with EPI readout at two distinct b-values (b=1000, b=2500 s/mm^2) along 120 encoding gradients that were uniformly distributed in space by an electrostatic repulsion approach [29]. This sequence is designed specifically to reduce the distortions induced by eddy currents in the diffusion-weighted images [30]. For the purposes of motion correction, 22 unweighted (b=0) volumes, interleaved with the DW images, were acquired. Volumes were acquired with a repetition time (TR) of 6800 ms, an echo time (TE) of 91 ms, and a field-of-view (FOV) of 211 mm^2. Maximum slew rate was 400 mT/(m/ms) and maximum gradient amplitude was 40 mT/m. No parallel imaging techniques were used. The multi-channel head coil was used to increase the signal-to-noise ratio, and not the speed of the acquisition. Volumes were acquired with a 6/8 partial Fourier factor. Voxels were isotropic with dimensions of 2.4 x 2.4 x 2.4 mm^3 and volumes were acquired in 54 transverse slices using an 88 x 88 voxel matrix. A high-resolution T1-weighted image was also acquired for each subject (3D modified driven equilibrium Fourier transform, repetition time = 7.92 ms, echo time = 2.4 ms, inversion time = 910 ms, flip angle = 15°, field of view = 256 x 224 x 176 mm^3, 1 mm isotropic spatial resolution).

Interleaved unweighted images from the diffusion sequence were realigned to the first unweighted volume with a rigid body transformation using SPM8 (Wellcome Trust Centre for Neuroimaging, UCL, UK). Registration was performed (rigid, mutual information) between the first unweighted volume and each of the interleaved unweighted volumes (e.g. register $b0_3$ to $b0_1$). The translation and rotation values between $b0_1$ and $b0_{22}$ were linearly interpolated and applied to the weighted volumes. This put all the weighted images in alignment with the first b0 volume without the contrast problems of co-registering weighted and unweighted images. Diffusion gradient vectors were rotated accordingly [31]. For each diffusion-weighted volume, a non-local mean filter was applied [32] and noise was corrected using power image correction adapted for multi-coil acquisitions [33]. No further corrections were applied to correct for eddy current-induced distortions in the diffusion-weighted volumes because the diffusion sequence did a sufficient job of suppressing them. Diffusion analysis in this study was performed exclusively on the volumes acquired at b=1000

s/mm^2.

T1-weighted structural meshing The structural meshing pipeline is an evolution of the "mri2mesh" Unix shell script provided in the Simulation of Non-invasive Brain Stimulation (SimNIBS, `http://simnibs.org/`) package [28]. The workflow begins with automated whole-brain segmentation of Freesurfer [34]. It relies on MeshFix [35] for repairing, dilating, merging, smoothing, remeshing, and otherwise modifying surface meshes of the various sections of the brain. Broadly, the segmented regions of grey matter, white matter, cerebrospinal fluid, skull, and skin are meshed in two dimensions and refined so that there are no intersections between the meshes of each tissue type. These 2D meshes are then processed using Gmsh [36] and used to create distinct 3D volume meshes for each tissue compartment. The FEM node closest to each of the EEG electrodes was obtained by computing the Euclidean distance between the sensor location and the nodes of the scalp mesh. Electrodes were saved in the Gmsh mesh file as new distinct physical volumes, so that they could be assigned as current sources during the forward modeling. Figure 2 shows the surface and volumetric meshes created for our subject alongside the original T1. The whole-head mesh contained 857,011 nodes and 5,916,850 tetrahedral elements.

Mapping conductivity tensors Tensors were fit at each voxel using linear least squares as implemented in the FMRIB Software Library [37] build 504. A fractional anisotropy map was generated and linear registration was performed to align the FA to the T1-weighted structural image. The tensors were then registered to the structural image using the calculated transformation matrix and rotated accordingly. Diffusion tensor eigenvalues were remapped to produce conductivity tensors [38] using functions from Dipy [39]. The primary eigenvectors and mean conductivity map were assessed to check that the tensors had proper orientation and magnitude.

In order to include the diffusion tensors in the finite element structural model, the centroid of all tetrahedrons in the white matter 3D mesh were computed, and their location in the volumetric conductivity tensor data was obtained. If the centroid of the element was within a voxel, and that voxel had a fractional anisotropy greater than or equal to 0.1, then the tensor within that voxel was assigned to the element. The fractional anisotropy threshold is

used solely to prevent inconsequential tensors from being included, and not to create a white matter mask. White matter elements whose centroids did not lie in a voxel (e.g. due to differing fields-of-view between the T1 and the DWI) were assigned isotropic conductivity values of 0.33 S/m. A coronal slice of the head model including the primary eigenvectors of the conductivity tensor can be found in Figure 3. The full conductivity tensor is taken into account within the finite element model calculations, not just the anisotropy or principal direction.

In Table 4 we recorded the clock time and disk usage required to process the described subject. These calculations were performed on a quad-core Xeon 2.6 GHz with 16 GB of RAM. The pipelines were run serially using a single CPU, and the total processing time was roughly 24 hours.

Isotropic vs. Anisotropic conductivity Two leadfields were created: one with isotropic conductivity (L_{iso}) within the white matter and another incorporating the conductivity tensors described above (L_{aniso}). These two leadfields were compared by computing the root mean square deviation (RMSD) between the leadfield components, for each sensor-sink pair, in every element (N) of the grey matter. The RMSD was computed for each direction (i) of the electric field, because we felt averaging would ignore clear directional effects induced by the brain's white matter structure. The reader should recall that M is list of EEG sensors.

$$RMSD^{N,i} = \frac{\sqrt{\sum_M (L_{iso}^{N,i} - L_{aniso}^{N,i})^2}}{||L_{iso}^{N,i}||} \tag{6}$$

This provides a method for visualizing the spatial distribution of the effects of anisotropic white matter conductivity on the leadfield matrix. Areas of high RMSD may be prone to source reconstruction errors in studies where isotropic conductivity is assumed.

Residual function mapping We further tested our forward model by calculating single-dipole residual fields for both the isotropic and anisotropic leadfields. The residual function relays the misfit between the scalp potential obtained from a pre-specified dipole and the potential that would be produced if optimally oriented dipoles were placed in each element.

First, a current dipole is placed inside one element and the "measured" scalp potential is obtained (Φ). Within each element, any dipole (j) will produce a

scalp potential ($\hat{\Phi}$) that can be derived from the pre-computed leadfield (L):

$$Lj = \hat{\Phi} \tag{7}$$

The optimal location of a single dipole can be found by minimization of the residual function (R):

$$R = (\hat{\Phi} - \Phi)^T (\hat{\Phi} - \Phi) \tag{8}$$

If $\hat{\Phi}$ is set to the measured potential (Φ), the best moment of this dipole is given by Equation 9.

$$j = L^+ \Phi \tag{9}$$

Where L^+ represents the Moore-Penrose pseudo-inverse ($L^+ = (L^T L)^{-1} L^T$) of the leadfield matrix. Since the optimal orientation can be calculated in this manner, the residual can be calculated as:

$$R = \hat{\Phi}^T [I - LL^+] \hat{\Phi} \tag{10}$$

The location of the global minimum of the residual function reflects the best guess for the position of the dipole within the mesh.

Results

The relative difference (RDM) and relative magnitude (MAG) between our method and the analytical solution across the 22 tested dipole positions can be found in Figure 5. Summary statistics calculated from these data points are available in Table 2.

We found that both our implementation and that of SimBio provide more spatially stable and accurate solutions than the boundary element approach available in OpenMEEG. At locations near the tissue boundaries (< 15 mm) the OpenMEEG solution differed substantially (RDM > 0.05) from the analytical solution, whereas both FEM approaches remained relatively accurate (RDM < 0.02). SimBio appears to be the most accurate approach overall as it marginally outperforms our implementation on both RDM and MAG.

Notable jaggedness is present in the RDM and MAG plots for the GetDP solution. This is because probe dipoles are snapped into the closest mesh elements (by Euclidean distance) in order to calculate the potential at the sensors. SimBio and OpenMEEG, in contrast, provide continuous solutions. This issue can be mitigated by reducing the characteristic length of the mesh elements (i.e. increasing mesh resolution) or widening the probe dipole sampling distance to a value larger than the characteristic length of the elements. In this case, we chose to place dipoles every 4 mm because our tetrahedra were defined with characteristic lengths of 3 mm.

In the human brain model, the incorporation of DWI-derived conductivity tensors substantially influenced the leadfield matrices that were created. The influence of incorporating anisotropic conductivity information into the leadfield matrix was most pronounced in regions connected by large fiber bundles. As shown in Figure 6, we found that the root mean squared deviation (RMSD) between the "isotropic" and "anisotropic" leadfields followed the pattern of major fiber tracts in the brain. Along the left-right axis (x direction), the largest RMSD between isotropic and anisotropic leadfields was found in grey matter regions connected by the corpus callosum. RMSD in the left-right axis was also particularly high in the precuneus and occipital lobe. Along the anterior-posterior axis (y direction), the largest RMSD was found near the anterior and posterior cingulate. Along the inferior-superior axis (z direction), the largest RMSD was found near the corticospinal tracts at both the mesencephalic and cortical levels. The left-right RMSD showed the highest mean (0.378) and widest deviation (0.237) between the isotropic and aniostropic leadfields, likely due to the influence of the corpus callosum. The influence of anisotropy, measured as the mean degree of error between leadfields, was smallest along the inferior-superior axis (0.295). Table 3 shows the influence of anisotropy by direction.

In Figure 7 the residual function fields for a dipole in the left superior frontal lobe are shown. The residual function in the leadfield with isotropic conductivity showed a wider distribution of low residual values throughout the brain and across hemispheres compared to the more realistic anisotropic head model. This lack of specificity in the isotropic head model is likely to result in errors when attempting to localize sources using an inverse solver.

Discussion

Here we have demonstrated a solution for calculating the EEG leadfield matrix using realistic, heterogeneous, and anisotropically conducting head models. The accuracy of the current forward modeling method was validated by its agreement with the analytical solution in a four-shell spherical model. The approach was found to be perform better than the current state-of-the-art symmetric BEM approach (OpenMEEG) and marginally worse than the only other available FEM implementation (SimBio). The ability to take into account anisotropic conductivity information was demonstrated with real human MRI data.

Two recent simulation studies have extended simple three-compartment head models to complex six-compartment models step-by-step to study the effects of modeling various aspects of the human head [8, 27]. Both studies also included anisotropic conductivity information derived from diffusion tensors. They found that anisotropic conductivity information has a strong effect on the EEG/MEG forward model, second only to the effect of including a separate CSF compartment and including distinct compartments for both grey and white matter [8].

It has now been established that current flows in the brain (e.g. following transcranial direct current stimulation) along trajectories parallel to the primary direction of the fiber tracts [4, 27]. Sources located deep in the brain, as well as those bordering strongly anisotropic tissue, are misrepresented in EEG localization when neglecting the effects of white matter anisotropy [4]. One recent study that included an inverse analysis found that sulcal sources localized in EEG studies may be mislocalized outside of the sulci if white matter anisotropy is neglected [6]. The dipole shift for these sources tended to be parallel to the principal direction of the nearby white matter. An earlier study estimated that ignoring white matter anisotropy could lead to dipole localization errors greater than 10 mm on average [3]. Our results show strong errors in the leadfield nearby large white matter tracts. Deviation between leadfields in all directions were more pronounced in sulci than gyri, reaffirming previously reported results [6]. Anisotropic conductivity information should not be ignored in neural source imaging studies.

While we have not yet integrated our approach with available inverse solvers, we have shown that our forward model is stable and accurate. The meshing

pipelines provided here may also prove useful for other types of finite-element simulations, such as those evaluating neurotrauma mechanics [40]. The finite element solution used during leadfield creation may also be adaptable for other types of simulations, such as the modeling of transcranial direct current stimulation. At present the toolbox is incapable of producing magnetoencephalography (MEG) leadfield matrices. Reciprocity solutions for MEG leadfields have been previously demonstrated [41], however, and this framework could be extended to allow for their creation.

Our approach contains many advantages over other competing methods. Whereas boundary element methods are usually restricted to nested shells [42], finite element methods allow for complex geometry in the head models. This means that an individual head model could be created, for example, for a patient with a hole, fracture, or implant in their skull. Furthermore, our FE mesh is of higher quality than many previous studies, as we use an unstructured tetrahedral mesh, rather than structured hexahedral grids (used in e.g. [27, 6]). This allows us to refine the mesh for more realistic calculations within highly curved regions of the brain. It may also be beneficial to implement anisotropy-adaptive mesh generation [43]. The non-uniformly tessellated mesh also sets the FEM approach apart from finite difference methods (FDM). One such finite difference reciprocity method has recently been demonstrated, though the publication only reports results in a head model with four distinct tissue types, and does not include realistic directional conductivity information [44].

There is one major electromagnetic property of the human head that we have overlooked in this study: the conductivity profile of the skull. Errors in skull segmentation are known to cause substantial issues in source localization [45]. The skull is actually composed of three layers: one layer of spongy bone encased by two layers of more compact bone, each with distinct conductivities [46]. Furthermore, it contains some air cavities (e.g. near the sinuses), and varies in thickness around the head [47]. It is also well known that the skull conducts faster radially than tangentially, leading to a smearing effect on the recorded scalp EEG [48]. It has recently been shown, however, that geometrical modeling errors of the skull have a larger effect on electromagnetic source localization than the conductivity model assigned to the skull region(s) [49]. At present our

implementation uses a simple single-shell skull with an isotropic conductivity of 0.0042 S/m (roughly $1/80^{th}$ that of the grey matter) [48]. Segmenting the skull into three compartments is difficult from T1-weighted MR images and additional sequences may be necessary. Future avenues for reducing localization error by improving the skull model are (i) including a three-layer model, and (ii) including tensor-based anisotropy measures based on radial and tangential skull conductivity measurements.

Skull and CSF segmentation guided by T1 and T2-weighted MRI is available in the processing pipelines (using BET [50, 51]), though they were not demonstrated specifically here. A comparison of FE models generated from a single T1-weighted image and an optimal set of four images (T1, T2, and fat-suppressed T1/T2 images) is available in the Supplementary Information. Qualitatively, the optimal set of images allows for more accurate segmentation, but the mesh generated from a single T1 image does appear to be of sufficient quality.

The primary disadvantage of our implementation versus those currently in use is the computational requirements and data storage cost. It is clear from our study and others, though, that accuracy in the conductivity model used for forward modeling is imperative for realistic source localization. Data storage issues for the triangular surface meshes may be mitigated in the future by incorporating entropy-reduction techniques and entropy encoding. One such available option is the OpenCTM format [52], which can losslessly encode triangular meshes to 5-6% of their size in the commonly used Standard Tessellation Language (STL) mesh format.

This work is a suitable basis for future finite element electromagnetic modeling studies of the human head. It performs quickly and with better accuracy than the current state-of-the-art boundary element modeling approach, and proves more stable near tissue boundaries. Its accuracy was found to be comparable to that of SimBio, a mature package for electromagnetic finite element modeling. Future work should interface this forward modeling approach with common EEG inverse solvers so the FEM approach becomes more widely adopted.

Technical Details

The source code behind this manuscript is available at the online repository service Github (`https://CyclotronResearchCentre.github.io/forward/`, GNU GPL v2 software license). Minimum recommended system requirements are a quad-core 2.0 GHz processor and 4 GB of RAM. Dependencies are Nipype [53], Dipy [39], the FMRIB Software Library [37], Gmsh [36], and GetDP [54]. The MRI data for the example subject demonstrated in this manuscript is automatically downloaded when running any of the examples in the software package.

Input data files for the software are high-quality T1-weighted magnetic resonance images. T1-weighted images should have previously been segmented using FreeSurfer[34], and the subject's white matter surfaces, pial surfaces, bias-corrected T1-weighted image, and segmented ROI map (using FreeSurferColorLUT labelling) should be available. If available, the pipelines will accept an additional T2-weighted image, or a set of four images (T1, T2 and fat-suppressed T1 and T2-weighted images), as in SimNIBS [28]. The tool will also accept diffusion-weighted images so that conductivity tensors can be derived for the subject. Diffusion preprocessing (e.g. correction for subject motion, eddy current-induced distortions, and table vibrations) should be performed prior to using the pipelines.

Primary output files are the leadfield matrix and volumetric head mesh (Gmsh MSH). The leadfield, which can become several hundred megabytes, depending on the mesh complexity, is stored as an HDF5 data file (The HDF Group. Hierarchical data format version 5, 2000-2010. `http://www.hdfgroup.org/HDF5`). Other outputs are the surface meshes of the skin, skull, cerebrospinal fluid, ventricles, grey matter, and white matter. Volumetric masks of the segmented structures are also provided in the NIfTI-1 data format. Part of this work included migrating the SimNIBS meshing scripts to use Nipype [53]. The provenance tracking in Nipype allows users to easily stop and restart the pipelines without any fear of lost data. This is enormously helpful for using and improving long-running, complex pipelines. Furthermore, Nipype allows jobs to be executed on distributed systems, such as cloud processing services, as well as locally on multi-core systems. The meshes created from the structural meshing pipeline can also be easily re-used in SimNIBS, if desired. If multimodal meshes

are to be included in place of the T1-derived mesh (e.g. the skull segmented from a CT scan), they must be centered at the RAS center (i.e. right, anterior, and superior are the positive x, y, and z directions) of the T1 image used for segmentation. The source code contains Gmsh example scripts for manually creating the 3D mesh file.

Acknowledgments

The authors would like to acknowledge the assistance of Axel Thielscher and André Antunes for the design of the software and Johannes Vorwerk for his guidance with SimBio.

References

[1] H. v. Helmholtz, Ueber einige gesetze der vertheilung elektrischer ströme in körperlichen leitern mit anwendung auf die thierisch-elektrischen versuche, Annalen der Physik 165 (6) (1853) 211–233.

[2] B. Vanrumste, G. Van Hoey, R. Van de Walle, R. D. Michel, I. A. Lemahieu, P. A. Boon, The validation of the finite difference method and reciprocity for solving the inverse problem in EEG dipole source analysis, Brain Topography 14 (2) (2001) 83–92.

[3] H. Hallez, B. Vanrumste, P. Van Hese, Y. D'Asseler, I. Lemahieu, R. Van de Walle, A finite difference method with reciprocity used to incorporate anisotropy in electroencephalogram dipole source localization, Physics in medicine and biology 50 (16) (2005) 3787.

[4] C. Wolters, A. Anwander, X. Tricoche, D. Weinstein, M. Koch, R. MacLeod, Influence of tissue conductivity anisotropy on EEG/MEG field and return current computation in a realistic head model: a simulation and visualization study using high-resolution finite element modeling, NeuroImage 30 (3) (2006) 813–826.

[5] M. Rullmann, A. Anwander, M. Dannhauer, S. K. Warfield, F. H. Duffy, C. H. Wolters, EEG source analysis of epileptiform activity using a 1 mm

anisotropic hexahedra finite element head model, NeuroImage 44 (2) (2009) 399–410.

[6] D. Güllmar, J. Haueisen, J. R. Reichenbach, Influence of anisotropic electrical conductivity in white matter tissue on the EEG/MEG forward and inverse solution. a high-resolution whole head simulation study., NeuroImage 51 (1) (2010) 145–163. doi:10.1016/j.neuroimage.2010.02.014.
URL http://dx.doi.org/10.1016/j.neuroimage.2010.02.014

[7] Y. Shirvany, T. Rubæk, F. Edelvik, S. Jakobsson, O. Talcoth, M. Persson, Evaluation of a finite-element reciprocity method for epileptic EEG source localization: Accuracy, computational complexity and noise robustness, Biomedical Engineering Letters 3 (1) (2013) 8–16.

[8] J. Vorwerk, J.-H. Cho, S. Rampp, H. Hamer, T. R. Knösche, C. H. Wolters, A guideline for head volume conductor modeling in EEG and MEG, NeuroImage In Press.

[9] V. Litvak, J. Mattout, S. Kiebel, C. Phillips, R. Henson, J. Kilner, G. Barnes, R. Oostenveld, J. Daunizeau, G. Flandin, et al., EEG and MEG data analysis in SPM8, Computational Intelligence and Neuroscience 2011 (2011) 852961–852961.

[10] Z. A. Acar, S. Makeig, Neuroelectromagnetic forward head modeling toolbox., Journal of Neuroscience Methods 190 (2) (2010) 258–270. doi:10.1016/j.jneumeth.2010.04.031.
URL http://dx.doi.org/10.1016/j.jneumeth.2010.04.031

[11] A. Gramfort, M. Luessi, E. Larson, D. A. Engemann, D. Strohmeier, C. Brodbeck, R. Goj, M. Jas, T. Brooks, L. Parkkonen, M. Hämäläinen, MEG and EEG data analysis with MNE-Python., Frontiers in Neuroscience 7 (2013) 267. doi:10.3389/fnins.2013.00267.
URL http://dx.doi.org/10.3389/fnins.2013.00267

[12] A. Gramfort, M. Luessi, E. Larson, D. A. Engemann, D. Strohmeier, C. Brodbeck, L. Parkkonen, M. S. Hämäläinen, MNE software for processing MEG and EEG data., NeuroImage 86 (2014) 446–460. doi:

10.1016/j.neuroimage.2013.10.027.
URL http://dx.doi.org/10.1016/j.neuroimage.2013.10.027

[13] A. Gramfort, T. Papadopoulo, E. Olivi, M. Clerc, OpenMEEG: opensource software for quasistatic bioelectromagnetics., BioMedical Engineering OnLine 9 (1) (2010) 45. doi:10.1186/1475-925X-9-45.
URL http://dx.doi.org/10.1186/1475-925X-9-45

[14] E. Olivi, T. Papadopoulo, M. Clerc, Handling white-matter anisotropy in BEM for the EEG forward problem, in: Biomedical Imaging: From Nano to Macro, 2011 IEEE International Symposium on, IEEE, 2011, pp. 799–802.

[15] J. Sarvas, Basic mathematical and electromagnetic concepts of the biomagnetic inverse problem, Physics in medicine and biology 32 (1) (1987) 11.

[16] d. J. Munck, M. J. Peters, A fast method to compute the potential in the multisphere model, IEEE transactions on biomedical engineering 40 (11) (1993) 1166–1174.

[17] F. Kariotou, Electroencephalography in ellipsoidal geometry, Journal of Mathematical Analysis and Applications 290 (1) (2004) 324–342.

[18] S. Vallaghé, T. Papadopoulo, M. Clerc, The adjoint method for general EEG and MEG sensor-based lead field equations, Physics in medicine and biology 54 (1) (2009) 135.

[19] P. H. Schimpf, C. Ramon, J. Haueisen, Dipole models for the EEG and MEG, Biomedical Engineering, IEEE Transactions on 49 (5) (2002) 409–418.

[20] C. H. Wolters, H. Köstler, C. Möller, J. Härdtlein, L. Grasedyck, W. Hackbusch, Numerical mathematics of the subtraction method for the modeling of a current dipole in EEG source reconstruction using finite element head models, SIAM Journal on Scientific Computing 30 (1) (2007) 24–45.

[21] S. Rush, D. A. Driscoll, EEG electrode sensitivity-an application of reciprocity, Biomedical Engineering, IEEE Transactions on (1) (1969) 15–22.

[22] D. Weinstein, L. Zhukov, C. Johnson, Lead-field bases for electroencephalography source imaging, Annals of biomedical engineering 28 (9) (2000) 1059–1065.

[23] D. Le Bihan, H. Johansen-Berg, Diffusion MRI at 25: exploring brain tissue structure and function, Neuroimage 61 (2) (2012) 324–341.

[24] D. S. Tuch, V. J. Wedeen, A. M. Dale, J. S. George, J. W. Belliveau, Conductivity tensor mapping of the human brain using diffusion tensor MRI., Proceedings of the National Academy of Sciences of the United States of America 98 (20) (2001) 11697–11701. doi:10.1073/pnas.171473898.
URL http://dx.doi.org/10.1073/pnas.171473898

[25] J. Fingberg, G. Berti, U. Hartmann, A. Basermann, F. Zimmermann, C. Wolters, A. Anwander, A. McCARTHY, S. Woods, Bio-numerical simulations with SimBio, NEC Research and Development 44 (1) (2003) 140–145.

[26] R. Oostenveld, P. Fries, E. Maris, J.-M. Schoffelen, FieldTrip: open source software for advanced analysis of MEG, EEG, and invasive electrophysiological data, Computational intelligence and neuroscience 2011 (2011) 156869–156869.

[27] S. Wagner, S. Rampersad, Ü. Aydin, J. Vorwerk, T. Oostendorp, T. Neuling, C. Herrmann, D. Stegeman, C. Wolters, Investigation of tDCS volume conduction effects in a highly realistic head model, Journal of Neural Engineering 11 (1) (2014) 016002.

[28] M. Windhoff, A. Opitz, A. Thielscher, Electric field calculations in brain stimulation based on finite elements: an optimized processing pipeline for the generation and usage of accurate individual head models., Human Brain Mapping 34 (4) (2013) 923–935. doi:10.1002/hbm.21479.
URL http://dx.doi.org/10.1002/hbm.21479

[29] D. K. Jones, M. A. Horsfield, A. Simmons, Optimal strategies for measuring diffusion in anisotropic systems by magnetic resonance imaging., Magnetic Resonance in Medicine 42 (3) (1999) 515–525.

[30] T. G. Reese, O. Heid, R. M. Weisskoff, V. J. Wedeen, Reduction of eddy-current-induced distortion in diffusion MRI using a twice-refocused spin echo., Magnetic Resonance in Medicine 49 (1) (2003) 177–182. doi:10.1002/mrm.10308.
URL http://dx.doi.org/10.1002/mrm.10308

[31] A. Leemans, D. K. Jones, The B-matrix must be rotated when correcting for subject motion in DTI data., Magnetic Resonance in Medicine 61 (6) (2009) 1336–1349. doi:10.1002/mrm.21890.
URL http://dx.doi.org/10.1002/mrm.21890

[32] M. Maggioni, V. Katkovnik, K. Egiazarian, A. Foi, Nonlocal transform-domain filter for volumetric data denoising and reconstruction., IEEE Transactions on Image Processing 22 (1) (2013) 119–133. doi:10.1109/TIP.2012.2210725.
URL http://dx.doi.org/10.1109/TIP.2012.2210725

[33] E. André, D, F. Grinberg, E. Farrher, I. I. Maximov, N. J. Shah, C. Meyer, M. Jaspar, V. Muto, C. Phillips, E. Balteau, Influence of noise correction on intra- and inter-subject variability of quantitative metrics in diffusion kurtosis imaging, PLoS ONE 9 (4) (2014) e94531. doi:10.1371/journal.pone.0094531.
URL http://dx.doi.org/10.1371%2Fjournal.pone.0094531

[34] R. S. Desikan, F. Ségonne, B. Fischl, B. T. Quinn, B. C. Dickerson, D. Blacker, R. L. Buckner, A. M. Dale, R. P. Maguire, B. T. Hyman, M. S. Albert, R. J. Killiany, An automated labeling system for subdividing the human cerebral cortex on MRI scans into gyral based regions of interest., NeuroImage 31 (3) (2006) 968–980. doi:10.1016/j.neuroimage.2006.01.021.
URL http://dx.doi.org/10.1016/j.neuroimage.2006.01.021

[35] M. Attene, A lightweight approach to repairing digitized polygon meshes, The Visual Computer 26 (11) (2010) 1393–1406.

[36] C. Geuzaine, J.-F. Remacle, Gmsh: A 3-D finite element mesh generator

with built-in pre-and post-processing facilities, International Journal for Numerical Methods in Engineering 79 (11) (2009) 1309–1331.

[37] S. M. Smith, M. Jenkinson, M. W. Woolrich, C. F. Beckmann, T. E. J. Behrens, H. Johansen-Berg, P. R. Bannister, M. D. Luca, I. Drobnjak, D. E. Flitney, R. K. Niazy, J. Saunders, J. Vickers, Y. Zhang, N. D. Stefano, J. M. Brady, P. M. Matthews, Advances in functional and structural MR image analysis and implementation as FSL., NeuroImage 23 Suppl 1 (2004) S208–S219. doi:10.1016/j.neuroimage.2004.07.051.
URL http://dx.doi.org/10.1016/j.neuroimage.2004.07.051

[38] A. Opitz, M. Windhoff, R. M. Heidemann, R. Turner, A. Thielscher, How the brain tissue shapes the electric field induced by transcranial magnetic stimulation., NeuroImage 58 (3) (2011) 849–859. doi:10.1016/j.neuroimage.2011.06.069.
URL http://dx.doi.org/10.1016/j.neuroimage.2011.06.069

[39] E. Garyfallidis, M. Brett, B. Amirbekian, A. Rokem, S. Van Der Walt, M. Descoteaux, I. Nimmo-Smith, Dipy, a library for the analysis of diffusion MRI data, Frontiers in Neuroinformatics 8 (2014) 8. doi:10.3389/fninf.2014.00008.
URL http://www.frontiersin.org/neuroinformatics/10.3389/fninf.2014.00008/abstract

[40] R. H. Kraft, P. J. Mckee, A. M. Dagro, S. T. Grafton, Combining the finite element method with structural connectome-based analysis for modeling neurotrauma: connectome neurotrauma mechanics, PLoS Computational Biology 8 (8) (2012) e1002619.

[41] P. H. Schimpf, Application of quasi-static magnetic reciprocity to finite element models of the MEG lead-field, IEEE Transactions on Biomedical Engineering 54 (11) (2007) 2082–2088.

[42] J. Kybic, M. Clerc, O. Faugeras, R. Keriven, T. Papadopoulo, Generalized head models for MEG/EEG: boundary element method beyond nested volumes, Physics in medicine and biology 51 (5) (2006) 1333.

[43] W. H. Lee, T.-S. Kim, Methods for high-resolution anisotropic finite element modeling of the human head: Automatic MR white matter anisotropy-adaptive mesh generation., Medical Engineering & Physics 34 (1) (2012) 85–98.

[44] G. Strobbe, P. van Mierlo, M. De Vos, B. Mijović, H. Hallez, S. Van Huffel, J. D. López, S. Vandenberghe, Bayesian model selection of template forward models for EEG source reconstruction, NeuroImage 93 (2014) 11–12.

[45] B. Lanfer, M. Scherg, M. Dannhauer, T. R. Knösche, M. Burger, C. H. Wolters, Influences of skull segmentation inaccuracies on EEG source analysis, NeuroImage 62 (1) (2012) 418–431.

[46] M. Akhtari, H. Bryant, A. Mamelak, E. Flynn, L. Heller, J. Shih, M. Mandelkem, A. Matlachov, D. Ranken, E. Best, et al., Conductivities of three-layer live human skull, Brain Topography 14 (3) (2002) 151–167.

[47] S. K. Law, Thickness and resistivity variations over the upper surface of the human skull, Brain Topography 6 (2) (1993) 99–109.

[48] S. Rush, D. Driscoll, Current distribution in the brain from surface electrodes., Anesthesia and analgesia 47 (6) (1968) 717.

[49] V. Montes-Restrepo, P. van Mierlo, G. Strobbe, S. Staelens, S. Vandenberghe, H. Hallez, Influence of skull modeling approaches on EEG source localization., Brain Topography 27 (1) (2014) 95–111. doi:10.1007/s10548-013-0313-y.
URL http://dx.doi.org/10.1007/s10548-013-0313-y

[50] S. M. Smith, Fast robust automated brain extraction, Human Brain Mapping 17 (3) (2002) 143–155.

[51] M. Jenkinson, M. Pechaud, S. Smith, BET2: MR-based estimation of brain, skull and scalp surfaces, in: Eleventh annual meeting of the Organization for Human Brain Mapping, Vol. 17, 2005.

[52] M. Geelnard. OpenCTM, the open compressed triangle mesh file format [online] (2010).

[53] K. Gorgolewski, C. D. Burns, C. Madison, D. Clark, Y. O. Halchenko, M. L. Waskom, S. S. Ghosh, Nipype: a flexible, lightweight and extensible neuroimaging data processing framework in Python., Frontiers in Neuroinformatics 5 (2011) 13. doi:10.3389/fninf.2011.00013.
URL http://dx.doi.org/10.3389/fninf.2011.00013

[54] P. Dular, C. Geuzaine, F. Henrotte, W. Legros, A general environment for the treatment of discrete problems and its application to the finite element method, Magnetics, IEEE Transactions on 34 (5) (1998) 3395–3398.

Figure Legends

Tables

Table 1: **Conductivity values and radii of the 4-shell spherical model.**

Shell	Radius (mm)	Conductivity (S/m)
Brain	85	0.33
Cerebrospinal Fluid	88	1.79
Skull	92	0.0042
Skin	100	0.33

Table 2: **Summary statistics of RDM and MAG**

Method	RDM	MAG
GetDP	0.013 (0.003)	1.033 (0.060)
OpenMEEG	0.125 (0.408)	1.345 (2.400)
SimBio	0.008 (0.002)	1.018 (0.031)

Summary of RDM and MAG values across varying dipole depths in the spherical model. Values represent mean (standard deviation) See Figure 5.

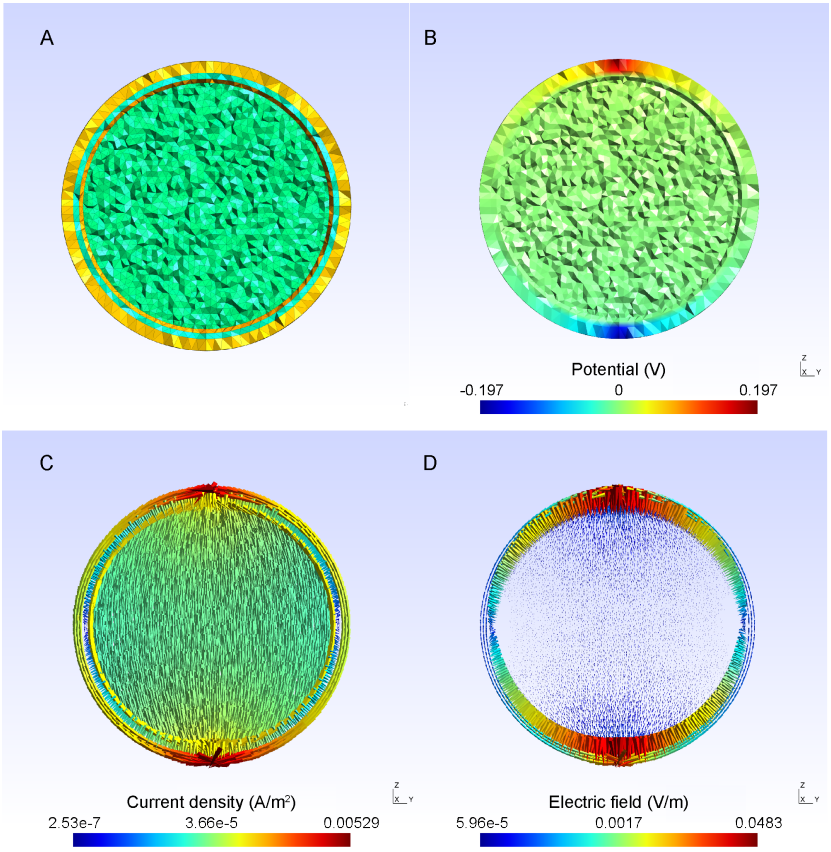

Figure 1: **Spherical mesh example.** A.) Sphere mesh geometry: Four-shell mesh including brain, CSF, skull, and scalp. B.) Potential distribution across the sphere (V): Single solution of the forward problem. Low potential is found at the sink electrode, and high potential is found at the current source. C.) Current density distribution (A/m^2), D.) Electric field distribution (Volts/m). Colours in C and D are on a logarithmic scale.

Table 3: **Summary statistics of RMSD between isotropic and anisotropic leadfields**

Direction	RMSD
Left-Right (X)	0.378 (0.237)
Anterior-Posterior (Y)	0.312 (0.188)
Inferior-Superior (Z)	0.295 (0.191)
Average	**0.328 (0.125)**

Summary of root mean squared deviation between leadfields created from meshes with isotropic white matter conductivity and anisotropic white matter conductivity tensors. Values represent mean (standard deviation) See Figure 6.

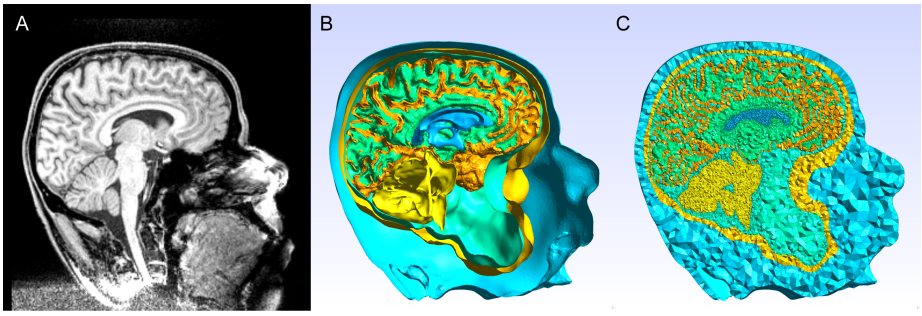

Figure 2: **Human head model.** A.) T1-weighted MRI image for our subject. B.) Surface meshes: The head model output from the structural meshing pipeline consists of several 2D shells representing the grey matter, white matter, cerebellum, ventricles, CSF, scalp, and skin. C.) 3D volume meshes. Volumetric meshes representing scalp (light blue), skull (bright yellow), ventricles (blue), cerebrospinal fluid (green), grey matter (orange), white matter (light green), and cerebellum (yellow) are created from the 2D shells.

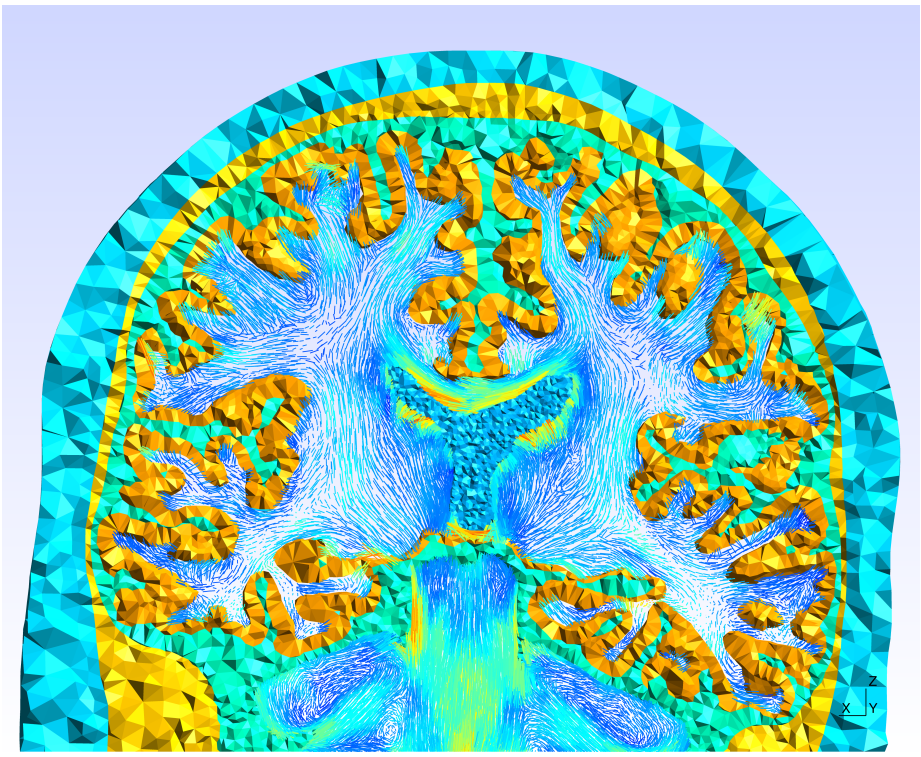

Figure 3: **Coronal slice of head model.** Primary eigenvectors of the conductivity tensor are shown within the white matter. The 3D grey matter (orange), cerebrospinal fluid (green), ventricles (blue), skull (yellow), and scalp (light blue) meshes are also shown.

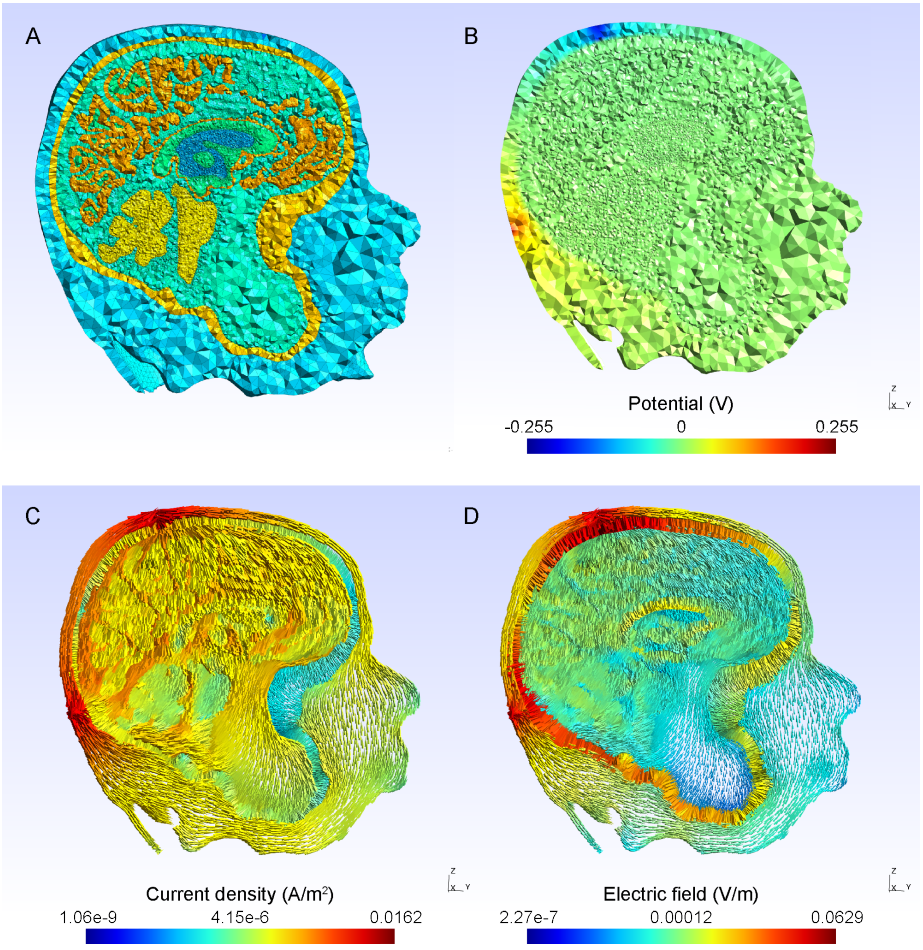

Figure 4: **Whole-head example** A.) Head model geometry: Four-shell mesh including brain, CSF, skull, and scalp. B.) Potential distribution throughout the head (V). C.) Current density distribution (A/m^2). D.) Electric field distribution (V/m). Colours in C and D are on a logarithmic scale.

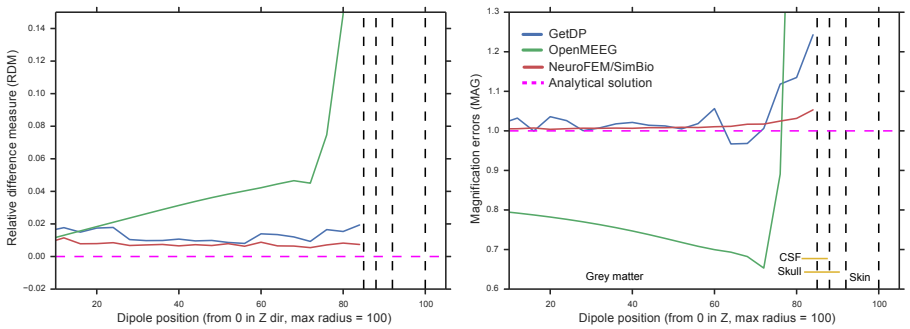

Figure 5: **Accuracy comparison between forward modeling methods.** Comparison between the relative difference measure (RDM) and relative magnitude (MAG) for our FEM reciprocity implementation (in blue), the FEM solution implemented in NeuroFEM/SimBio (in red), and the symmetric BEM solution implemented in OpenMEEG [13] (in green). The horizontal pink dashed line shows the analytical solution. Vertical black dashed lines show the boundaries between tissue shells.

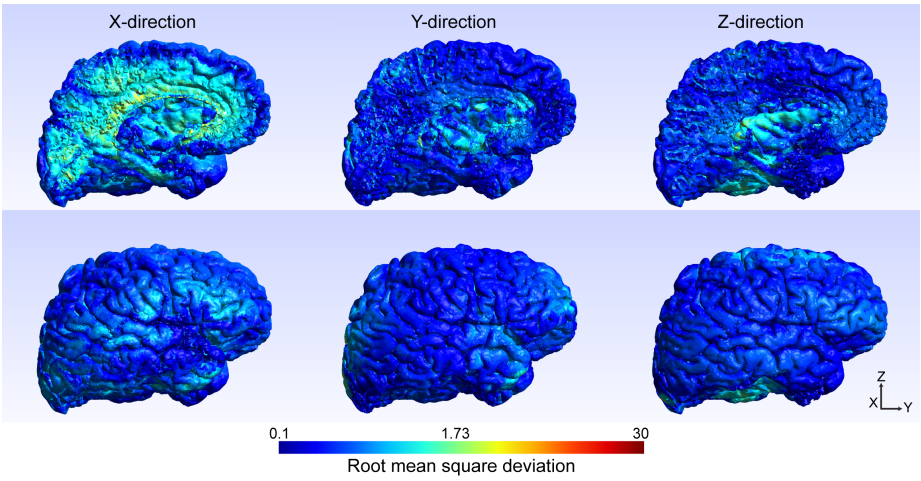

Figure 6: **Root mean square deviation between leadfields created with and without white matter conductivity tensors.** Leadfield root mean square deviation maps show the influence of including white matter conductivity tensors on the created leadfield matrices. Colour is on a logarithmic scale.

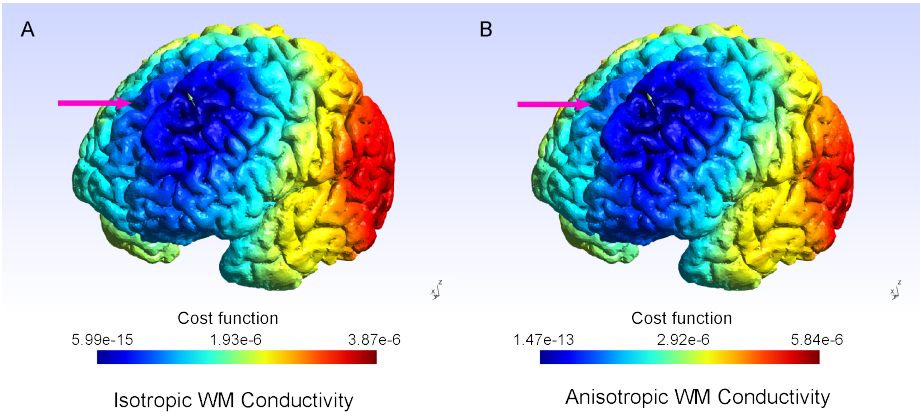

Figure 7: **Single-dipole residual fields** Residual field for A.) the leadfield with isotropic WM conductivity, and B.) the leadfield including realistic WM conductivity tensors. The residual field is calculated by placing a single dipole within the mesh, and then obtaining the difference between the scalp potential produced by this dipole, and the potential produced by an optimal dipole placed in each other element, individually. The minimum of this field represents the dipole position. As shown by the pink arrows, the residual minima bleed further into the opposite hemisphere within the isotropic leadfield, compared to the more realistic conductivity model.

Table 4: **Computational cost and storage required for each step.**

Task	Time (HH:MM:SS)	Disk Usage (GB)
Initial reconstruction	14:16:16	0.4
Structural meshing	04:05:11	2.4
Diffusion tensor processing	00:36:35	0.9
Electrode incorporation	00:01:00	0.6
Leadfield creation	04:21:17	19.5
Total	**23:20:19**	**23.8**

Initial reconstruction was performed with FreeSurfer 5.3 using the "recon-all" command with the option "–autorecon-all"